Supplementary Information

Chloride-Induced Easier Phase Transformation and Catalytic Synergy for Enhanced Seawater Splitting

Haibin Ma, Yuxiang Jin, Xiaoyan Zhou, Yujie Cui, Yang Zhao, Chia-Yu Chang, Min-Hsin Yeh, Wei-Hsiang Huang, Erhong Song*, Jiwei Ma*, Hongfei Cheng**

H. Ma, X. Zhou, Y. Cui, J. Ma, H. Cheng

School of Materials Science and Engineering, Tongji University, Shanghai 201804, P. R. China.

E-mail: jiwei.ma@tongji.edu.cn, cheng_hongfei@tongji.edu.cn

Y. Jin, E. Song

Key Laboratory of Automobile Materials, School of Materials Science and Engineering, Jilin University, Changchun 130025, P. R. China.

Y. Zhao

Dalian National Laboratory for Clean Energy (DNL), Dalian Institute of Chemical Physics, Chinese Academy of Science, Dalian 116023, P. R. China.

C.-Y. Chang

Graduate Institute of Applied Science and Technology, National Taiwan University of Science and Technology, Taipei 106, Taiwan.

M.-H. Yeh

Department of Chemical Engineering, National Taiwan University of Science and Technology, Taipei 106, Taiwan.

W.-H. Huang

Sustainable Electrochemical Energy Development (SEED) Center, National Taiwan University of Science and Technology, Taipei 106, Taiwan.

National Synchrotron Radiation Research Center (NSRRC), Hsinchu, 300092, Taiwan.

Email: huang.sean@nsrrc.org.tw

E. Song

State Key Laboratory of High Performance Ceramics, Shanghai Institute of Ceramics, Chinese Academy of Sciences, Shanghai 201899, P. R. China.

Email: ehsong@mai.sic.ac.cn

Experimental Section

Materials synthesis

1). Synthesis of α-$Co(OH)_2$: The α-$Co(OH)_2$ nanosheets grown on nickel foam (NF) were prepared by electrodeposition. Prior to the deposition, a piece of NF (1 cm × 1cm) was carefully cleaned by 1.0 M HNO_3 aqueous solution, deionized water and ethanol for several times, respectively. Then the electrochemical deposition with a three-electrode system (utilizing the pre-cleaned NF, platinum gauze and saturated calomel electrode as the working, counter and reference electrodes, respectively) was conducted in a 0.02 M $Co(NO_3)_2$ aqueous solution containing 10 mL 0.1 M NH_4Cl at the geometric current density of -2 mA cm^{-2} for 2 h.

2). Synthesis of RuO_x/α-$Co(OH)_2$: RuO_x nanoclusters decorated on the as-prepared α-$Co(OH)_2$ nanosheets by a wet-chemistry impregnation method. Typically, the α-$Co(OH)_2$ was immersed in 12 mL 2.0 mM $RuCl_3$ aqueous solution at room temperature for 30 min. After washed by deionized water and ethanol for several times, the final product RuO_x/α-$Co(OH)_2$ was obtained.

3). Synthesis of IrO_x/α-$Co(OH)_2$: IrO_x nanoclusters decorated on the as-prepared α-$Co(OH)_2$ nanosheets by the same wet-chemistry impregnation method. Typically, the α-$Co(OH)_2$ was immersed in 12 mL 2.0 mM $IrCl_3$ aqueous solution at room temperature for 30 min. After washed by deionized water and ethanol for several times, the final product IrO_x/α-$Co(OH)_2$ was obtained.

4). Synthesis of Ru-IrO_x/α-$Co(OH)_2$: The α-$Co(OH)_2$ nanosheets decorated with Ru-doped IrO_x nanoclusters were fabricated by the same wet-chemistry impregnation method. Typically, the α-$Co(OH)_2$ was immersed in 12 mL 1.67 mM $IrCl_3$ and 0.33 mM $RuCl_3$ mixed aqueous solution at room temperature for 30 min. After washed by deionized water and ethanol for several times, the final product Ru-IrO_x/α-$Co(OH)_2$ was obtained. Other Ru-IrO_x/α-$Co(OH)_2$ samples with different IrO_x/RuO_x loading amount were also prepared by changing the molar ratio of Ir^{3+}/Ru^{3+} ions in the wet-chemistry impregnation synthesis while keeping the total concentration of Ir^{3+} and Ru^{3+} ions as constant.

Materials characterizations

The microstructures and nanostructures of all the catalysts were characterized by scanning electron microscopy (SEM, JSM-6700F, 5 keV) and transmission electron microscopy (TEM, JEOL JEM-2100F, 200 keV) equipped with an energy diffraction microscopy (EDS). X-ray photoelectron

spectroscopy (XPS) was performed on a thermal ECSALAB 250 (150 keV, 6 mA) with an Al anode. All the charge states were compensated by shifting binding energies based on the C 1s peak (284.8 eV). The concentration of metal ions in electrodes was determined by the inductively coupled plasma optical emission spectrometer (ICP-OES, Varian 710-ES). X-ray diffraction (XRD) pattern was performed on a Bruker D8 Advance powder diffractometer (operated under 40 mA and 40 kV) equipped with a Cu-Kα source (λ_1 = 1.5405 Å, λ_2 = 1.5443 Å) at room temperature.

Electrochemical measurements

The alkaline sea water oxidation performances were tested in a traditional three-electrode system using platinum gauze and normal calomel as the counter and reference electrodes, respectively. Before recording the polarization curves, all the samples were activated by the cyclic voltammetry (CV) test at 10 mV s^{-1}. The electrochemical impedance spectroscopy (EIS) was conducted at the potential of 1.51 V (vs. RHE) from 100 kHz to 0.01 Hz. All the electrochemical data for OER were obtained by 85% iR-compensation. The long-term stability for alkaline seawater oxidation and overall sea water splitting was operated under chronopotentiometry mode at different current densities. The electrochemical double layer capacitance (C_{edl}) was calculated by measuring the non-Faradaic capacitive from a series of CV curves at different scan rates (10, 20, 30, 40 mV s^{-1}).

AEMWE evaluation

The anion exchange membrane water electrolysis (AEMWE) was assembled to evaluate the potential of Ru-IrO_x/α-$Co(OH)_2$ for industrial application. Ru-IrO_x/α-$Co(OH)_2$ was synthesized on Ti foam (10*10*0.5 mm) to serve as the anode and commercial Pt/C catalyst (loading: 1 mg cm^{-2}) was sprayed on carbon paper to serve as the cathode. Ti foam and carbon paper acted as the gas diffusion layers. The anion exchange membrane (AEM02-80 μm, Kah Membrane Technology) was soaked in 1 M KOH solution for 4 h at room temperature and then placed at the center of anode and cathode. Two pieces of polymeric soft spacers was symmetrically adjacent to the anode and cathode and two pieces of Ti plates was symmetrically adjacent to the polymerica soft spacers. The alkaline seawater electrolyzer was peristaltically pumped into the AEMWE device with flow rate of 30 mL min^{-1}. The AEMWE activity was evaluated using cyclic voltammetry method, and the AEMWE stability was evaluated under constant current density at constant temperature for long-term electrolysis.

Calculation of electrochemical surface area

The electrochemical surface area (ECSA) was determined by: $ECSA = C_{dl}/C_s$, where C_{dl} is double-layer capacitance and C_s the specific capacitance of the sample. In this study, a general specific capacitance value of $C_s = 0.035$ mF cm^{-2} was used based on typical reported values.[1-2]

Calculation methods

All DFT calculations were done in the Vienna Ab initio simulation package (VASP) with the performed Perdew-Burke-Ernzerhof's Generalized Gradient Approximation (GGA-PBE) function. The cut-off energy was set to 450 eV. And the spin polarization considered in the DFT calculations was based on the plane-wave basis set. The Brillouin zone was sampled with a 4 × 4 × 1 k-point grid using the Monkhorst-Pack method, whereas a dense 10 × 10 × 1 k-point grid was used for electronic property calculations. The structure was optimized with an energy convergence criterion of 10^{-4} eV and a force convergence criterion of 0.01 eV Å^{-1}. The vacuum space more than 10 Å was added along the Z-axis to eliminate the effects of symmetry. Correction of weak dispersion interactions during surface adsorption was performed by Grimme's DFT-D3 method. The Crystal Orbital Hamilton Population (COHP) was calculated by the Lobster package. COHP was used to investigate the bond strength between cobalt, iridium and ruthenium d-orbitals and oxygen p-orbitals.

The adsorption energy was calculated as follows:

$$E_{ads} = E_{total} - E_{slab} - E_{Cl^-}$$

E_{total} corresponded to the energies of the total energy of the catalyst adsorbed with one Cl^- ion. Where the E_{slab} and E_{Cl^-} were the energies of catalyst and half of Cl_2, respectively.

The ClER process in an alkaline medium could be described as follows:

$$* + Cl^- \rightarrow *Cl + e^-, \Delta G1$$

$$*Cl + Cl^- \rightarrow * + Cl_2 + e^-, \Delta G2$$

The OER process in an alkaline medium could be described as follows:

$$* + OH^- \rightarrow *OH + e^-, \Delta G1$$

$$*OH + OH^- \rightarrow *O + H_2O + e^-, \Delta G2$$

$$*O + OH^- \rightarrow *OOH + e^-, \Delta G3$$

$$*OOH + OH^- \rightarrow * + O_2 + H_2O + e^-, \Delta G4$$

And the theoretical overpotential (η_{OER}) was usually computed as:

$$\eta_{OER} = \max \{\Delta G1, \Delta G2, \Delta G3, \Delta G4\} - 1.23$$

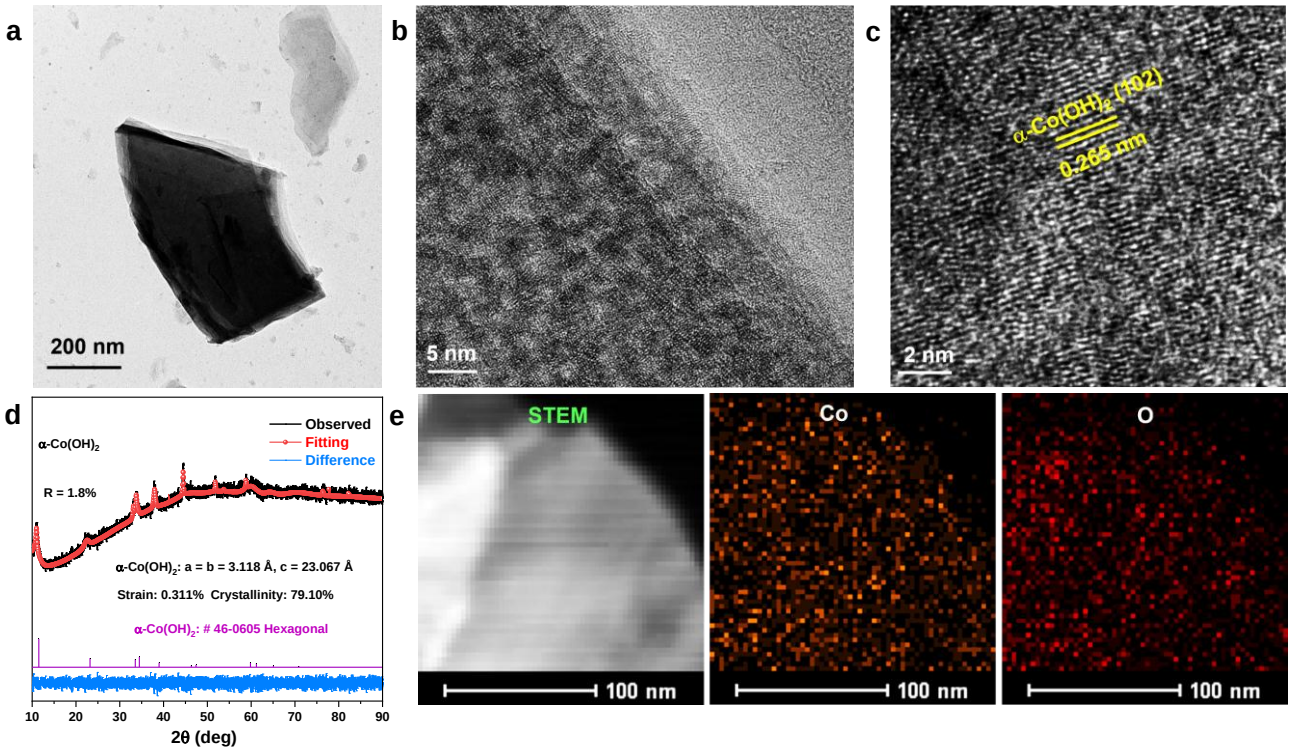

Figure S1. (a) TEM image of α-$Co(OH)_2$ nanosheets. (b,c) HRTEM images of α-$Co(OH)_2$ nanosheets. (d) XRD pattern of α-$Co(OH)_2$ catalyst. (e) STEM image and corresponding EDS mappings of α-$Co(OH)_2$ nanosheets.

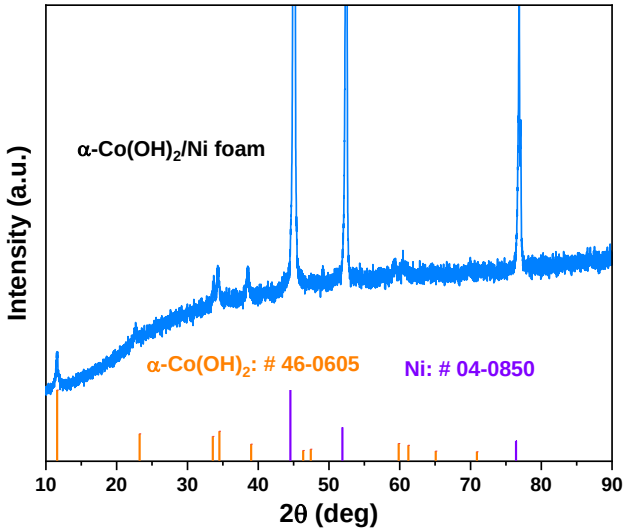

Figure S2. XRD pattern of α-$Co(OH)_2$ nanosheets grown on nickel foam using electrodeposition method.

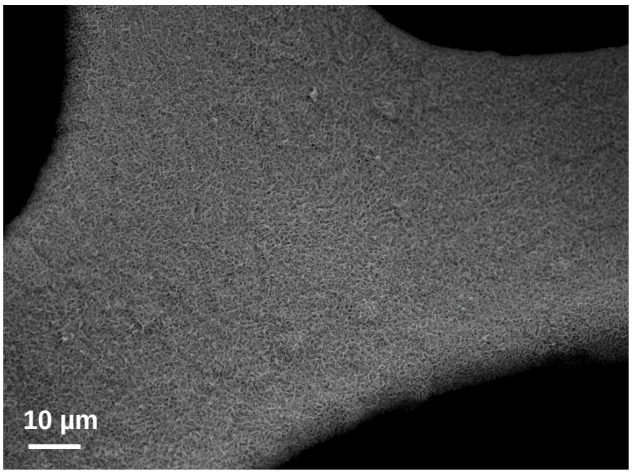

Figure S3. SEM image of Ru-IrO_x/α-$Co(OH)_2$ catalyst.

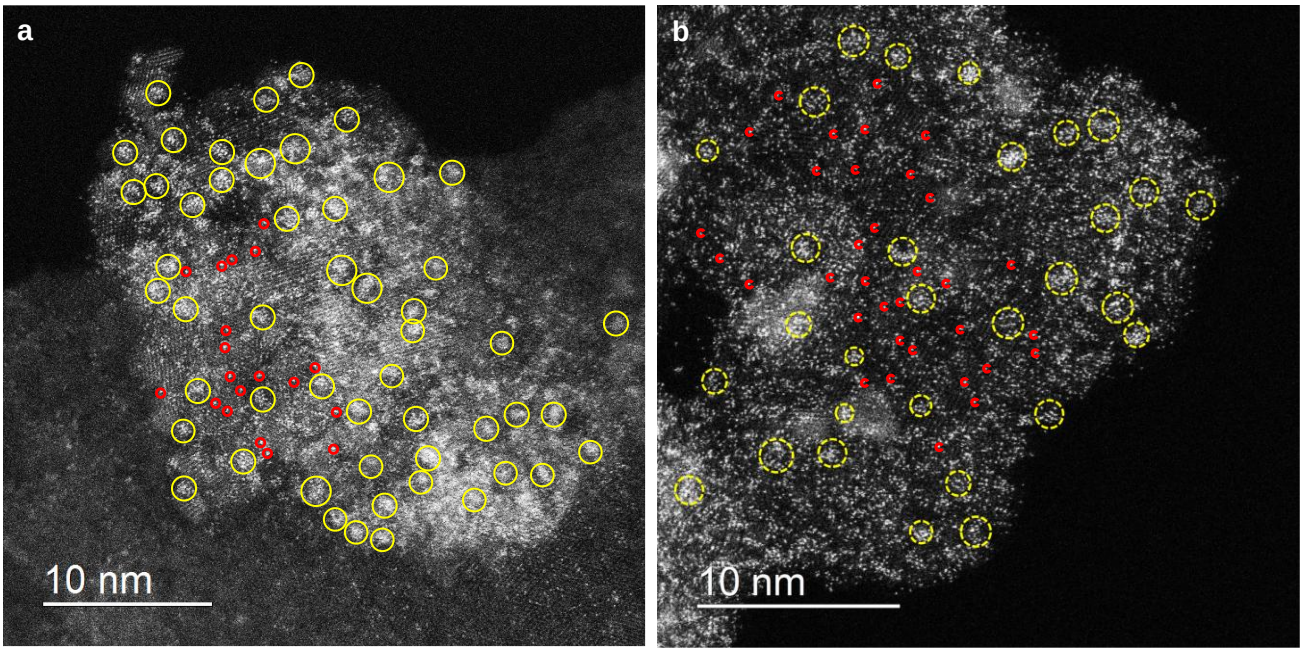

Figure S4. (a,b) HAADF-STEM images of Ru-IrO_x/α-$Co(OH)_2$ catalyst.

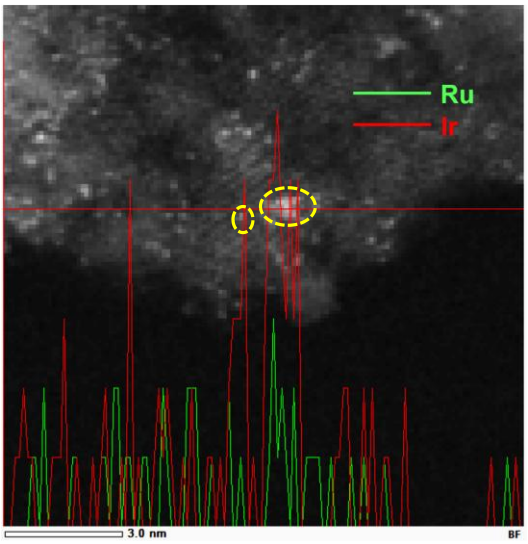

Figure S5. EDS line scan profile for Ru-IrO_x/α-$Co(OH)_2$ catalyst.

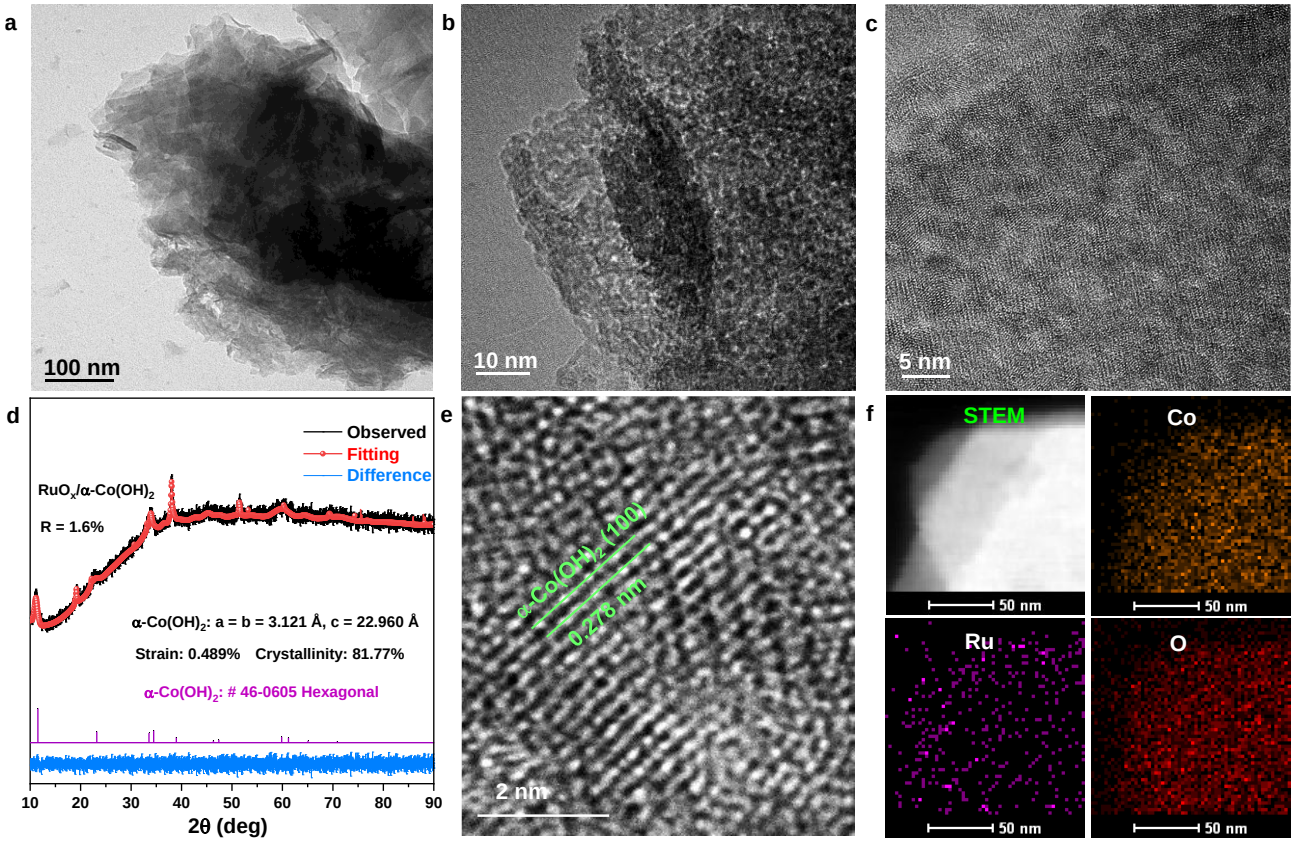

Figure S6. (a,b) TEM images of RuO_x/α-$Co(OH)_2$ catalyst. (c) HRTEM image of RuO_x/α-$Co(OH)_2$ catalyst. (d) XRD pattern of RuO_x/α-$Co(OH)_2$ catalyst. (e) HRTEM image of RuO_x/α-$Co(OH)_2$ catalyst. (f) STEM image of RuO_x/α-$Co(OH)_2$ catalyst and corresponding EDS mappings of Co, Ru and O elements.

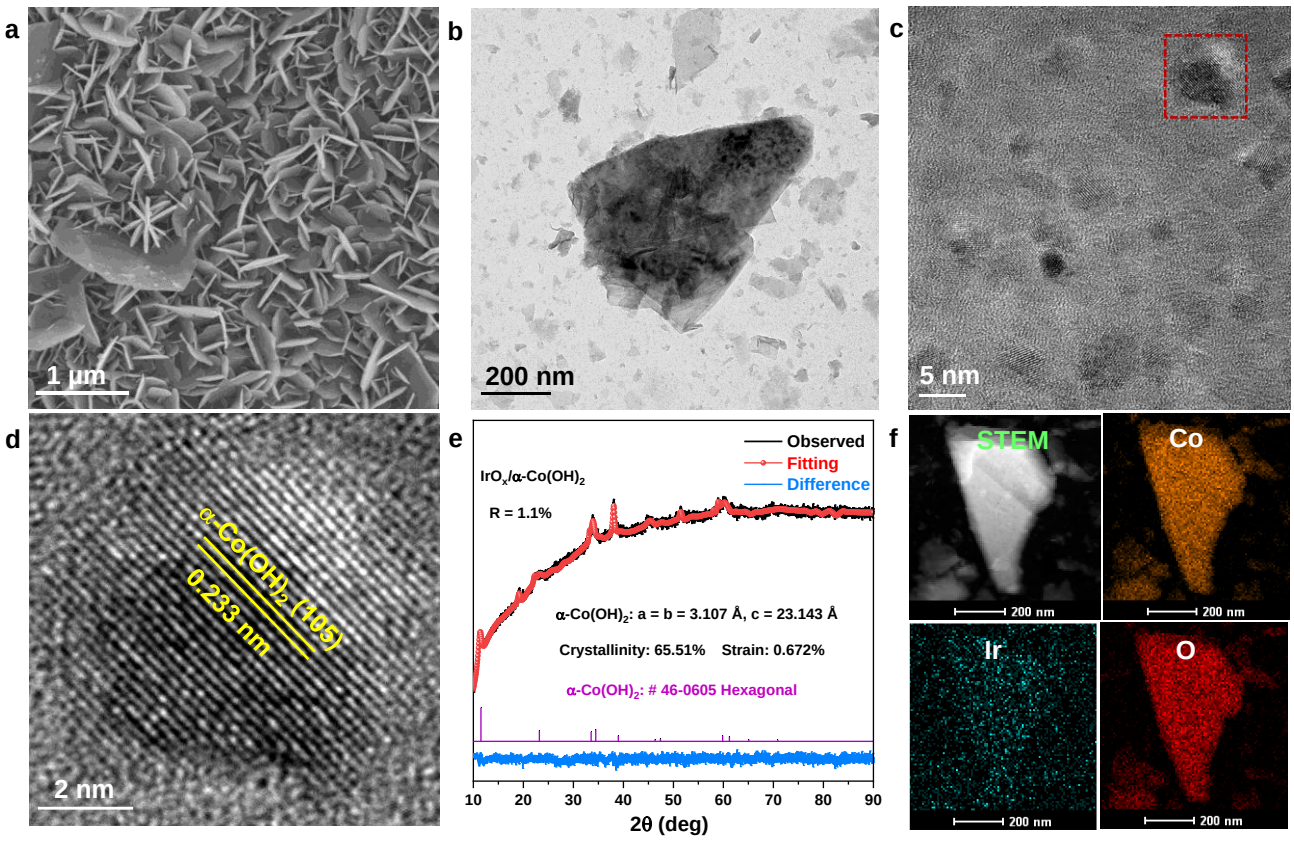

Figure S7. (a) SEM image of IrO_x/α-$Co(OH)_2$ catalyst, displaying the nanosheet array morphology. (b) Low-magnefication TEM image of IrO_x/α-$Co(OH)_2$ catalyst. (c) HRTEM image of IrO_x/α-$Co(OH)_2$ catalyst. (d) Enlarged HERTEM image of the area marked in (d). (e) XRD pattern of IrO_x/α-$Co(OH)_2$ catalyst. (f) STEM image of IrO_x/α-$Co(OH)_2$ catalyst and corresponding EDS mappings of Co, Ir and O elements.

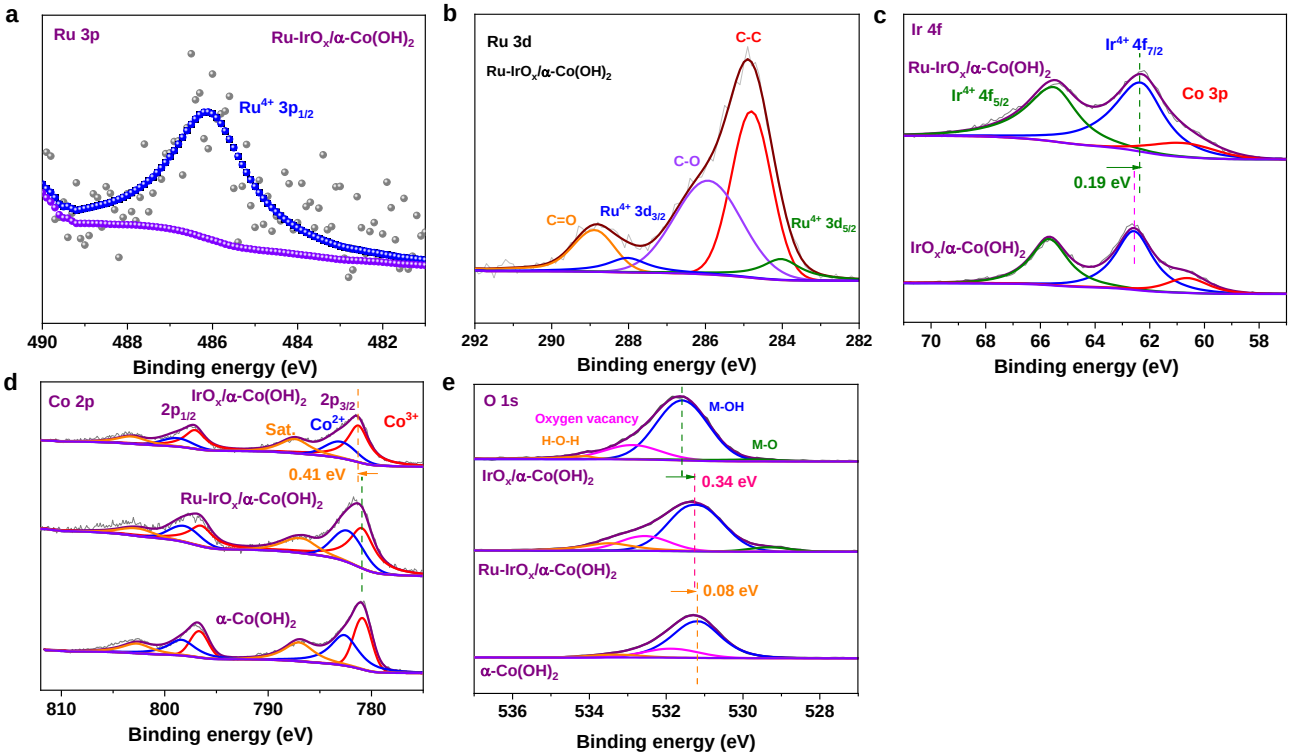

Figure S8. (a) Ru 3p XPS spectrum of Ru-IrO_x/α-$Co(OH)_2$ catalyst. (b) Ru 3d XPS spectrum of Ru-IrO_x/α-$Co(OH)_2$ catalyst. (c) Ir 4f XPS spectra of Ru-IrO_x/α-$Co(OH)_2$ and IrO_x/α-$Co(OH)_2$ catalysts. (d) Co 2p XPS spectra of Ru-IrO_x/α-$Co(OH)_2$, IrO_x/α-$Co(OH)_2$ and α-$Co(OH)_2$ catalysts. (e) O 1s XPS spectra of IrO_x/α-$Co(OH)_2$, Ru-IrO_x/α-$Co(OH)_2$ and α-$Co(OH)_2$ catalysts.

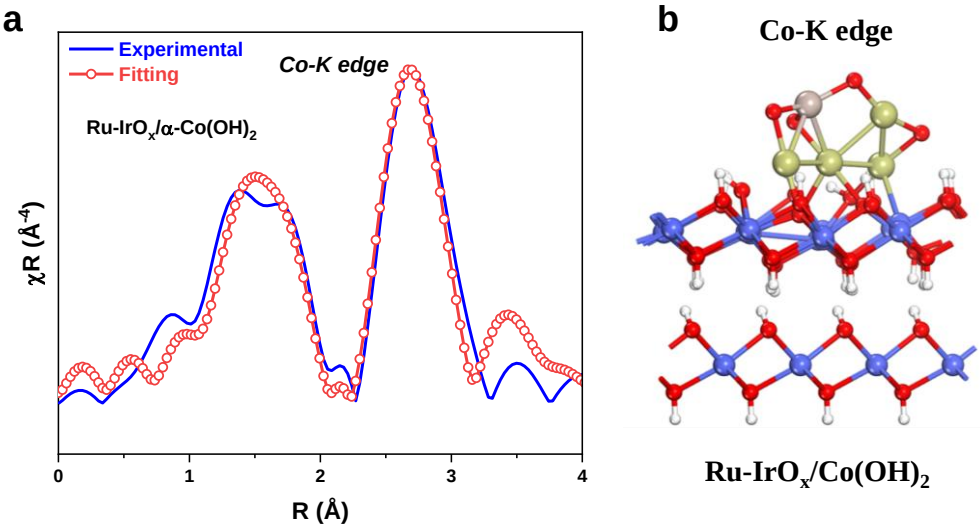

Figure S9. (a) Fitting curve for Co-K edge EXAFS spectra of Ru-IrO_x/α-$Co(OH)_2$. (b) The reference model Ru-IrO_x/$Co(OH)_2$ used for Co-K edge fitting.

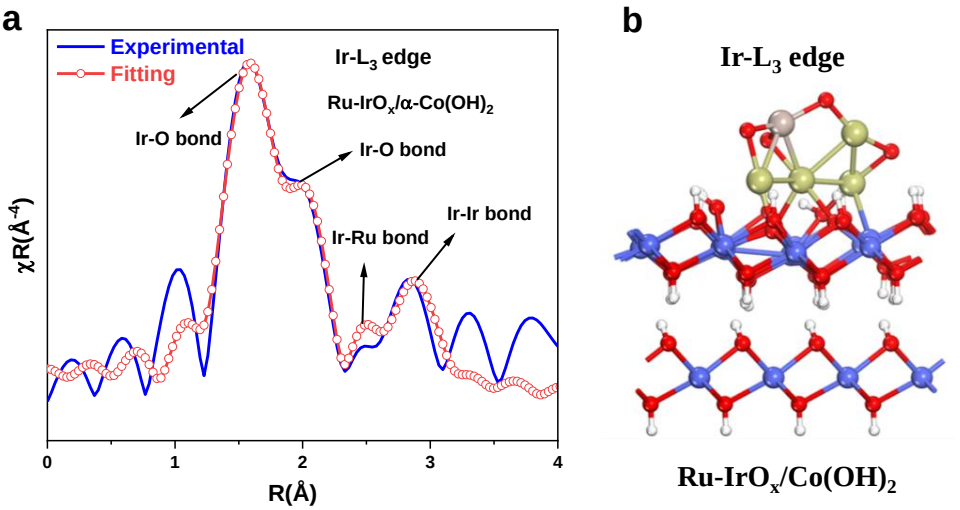

Figure S10. (a) Fitting curve for Ir-L_3 edge EXAFS spectra of Ru-IrO_x/α-$Co(OH)_2$. (b) The reference model Ru-IrO_x/$Co(OH)_2$ used for Ir-L_3 edge fitting.

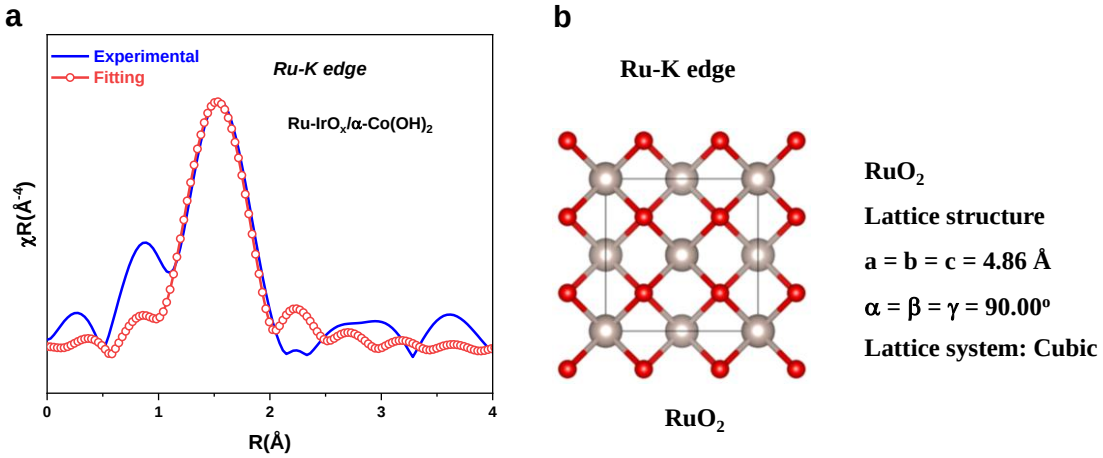

Figure S11. (a) Fitting curve for Ru-K edge EXAFS spectra of Ru-IrO_x/α-$Co(OH)_2$. (b) The reference model cubic RuO_2 used for Ru-K edge fitting.

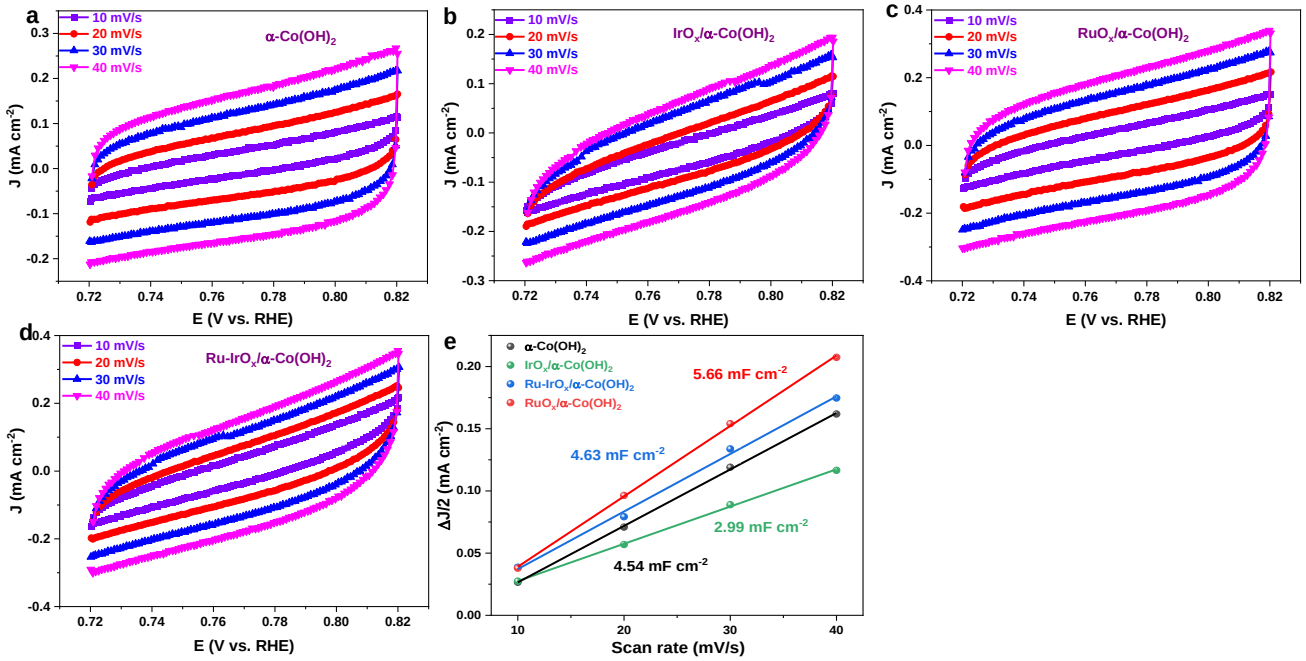

Figure S12. Electrochemical double layer capacitance (C_{edl}) evaluation. Cyclic voltammograms in the potential window from 0.72 V to 0.82 V (vs. RHE) at different scan rates for (a) α-$Co(OH)_2$, (b) IrO_x/α-$Co(OH)_2$, (c) RuO_x/α-$Co(OH)_2$, (d) Ru-IrO_x/α-$Co(OH)_2$ catalysts. (e) Current density differences plotted against different scan rates of α-$Co(OH)_2$, IrO_x/α-$Co(OH)_2$, RuO_x/α-$Co(OH)_2$, Ru-IrO_x/α-$Co(OH)_2$ electrodes. C_{edl} is equivalent to the slope of fitted line.

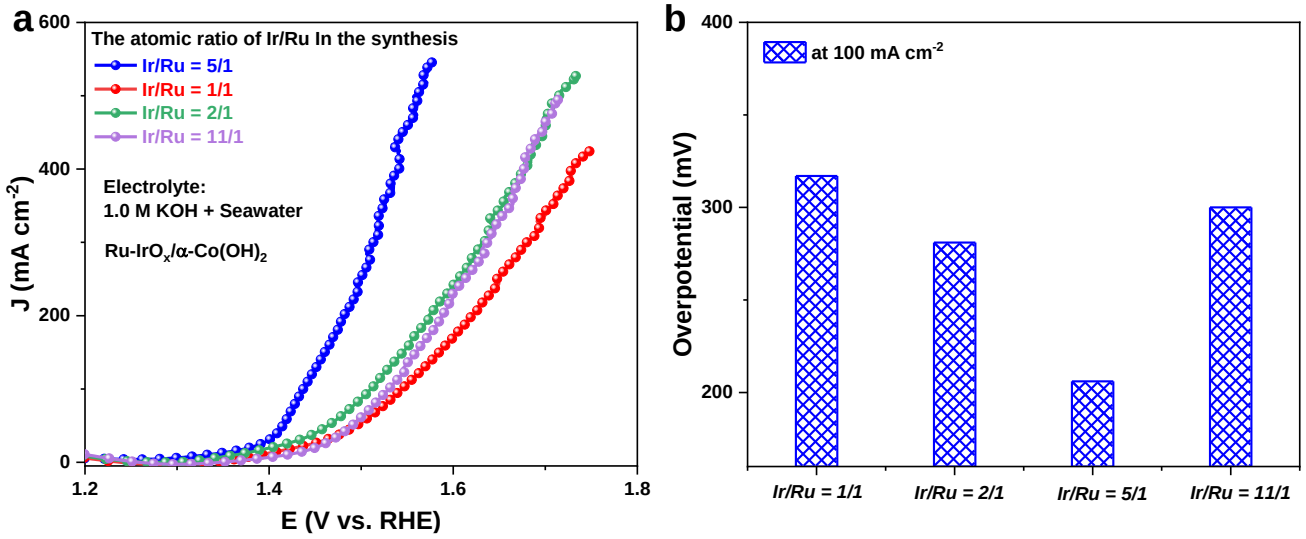

Figure S13. Electrochemical performance evaluation in 1.0 M KOH + seawater electrolyte. (a) LSV curves, (b) Overpotential comparison of Ru-IrO_x/α-$Co(OH)_2$ catalysts synthesized with different atomic ratios of Ir/Ru species.

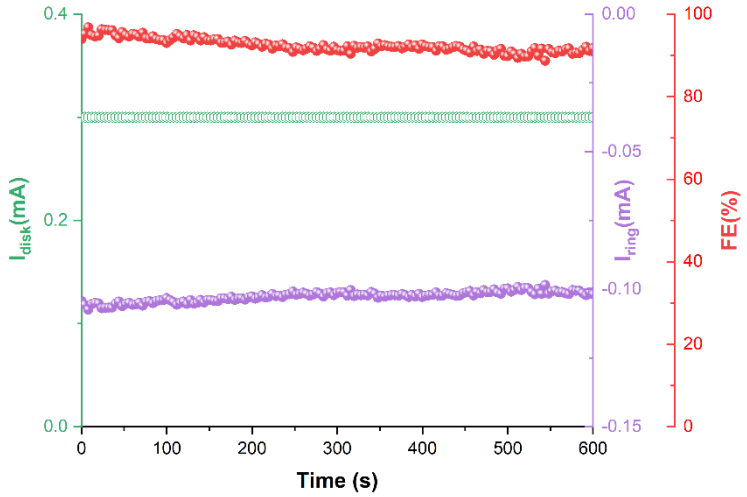

Figure S14. Faraday efficiency of Ru-IrO_x/$Co(OH)_2$ catalyst in 1M KOH + seawater.

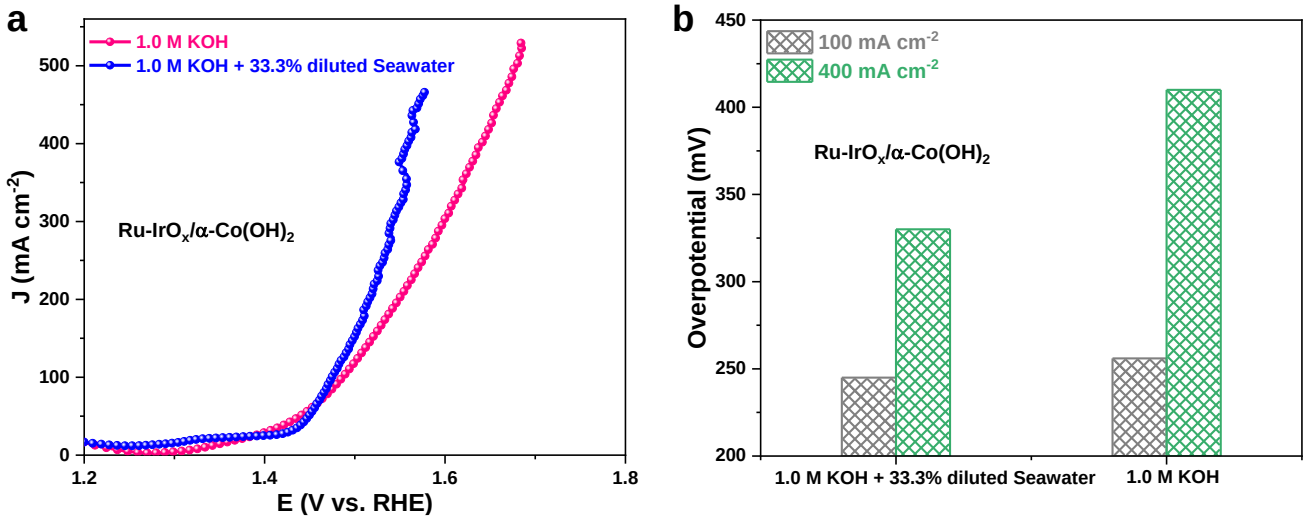

Figure S15. Electrochemical performance comparison in different electrolytes. (a) LSV curves of Ru-IrO_x/α-$Co(OH)_2$ catalyst in 1.0 M KOH + 33.3% diluted seawater and 1.0 M KOH electrolytes. (b) Overpotential comparison of Ru-IrO_x/α-$Co(OH)_2$ catalyst in the above two electrolytes at 100 and 400 mA cm^{-2}.

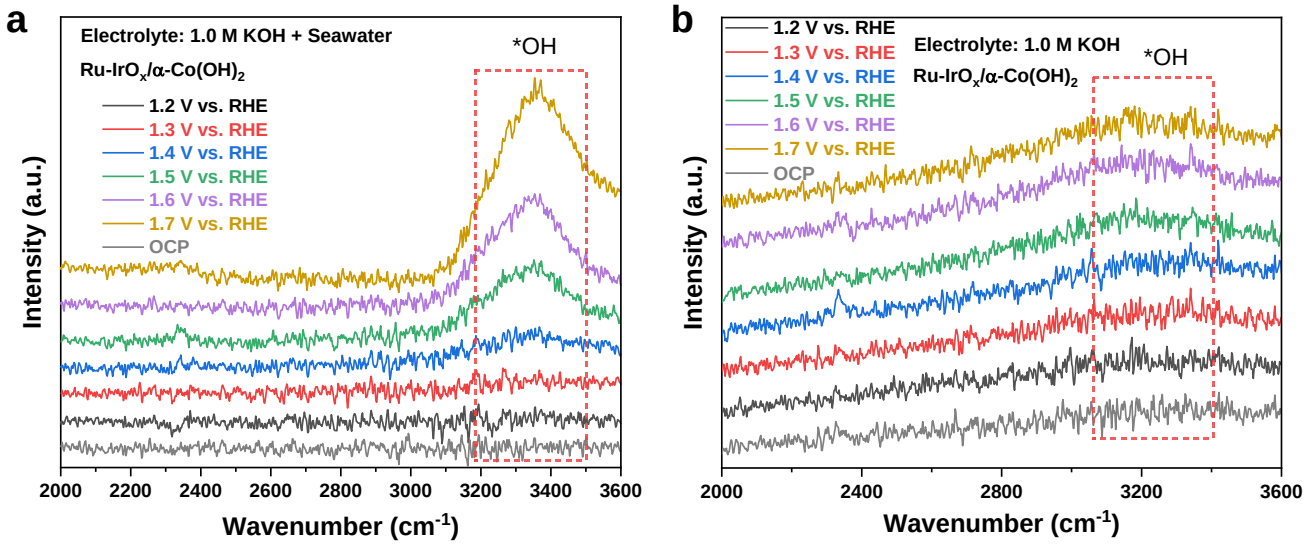

Figure S16. Comparison for the in-situ FTIR spectra of Ru-IrO$_x$/α-Co(OH)$_2$ catalyst operating in the electrolytes of (a) 1.0 M KOH + seawater and (b) 1.0 M KOH.

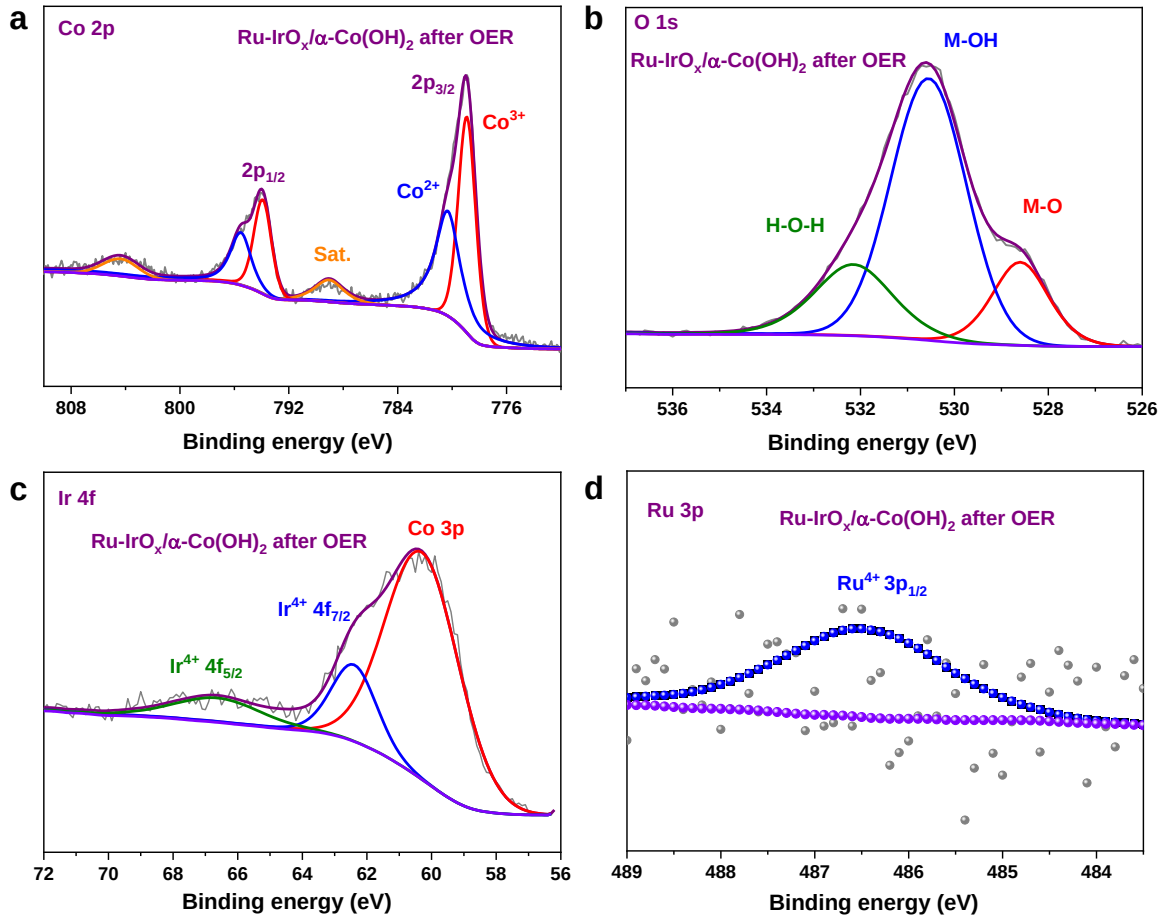

Figure S17. High-resolution (a) Co 2p, (b) O 1s, (c) Ir 4f, (d) Ru 3p XPS spectra of Ru-IrO$_x$/α-Co(OH)$_2$ catalyst after alkaline seawater oxidation stability test.

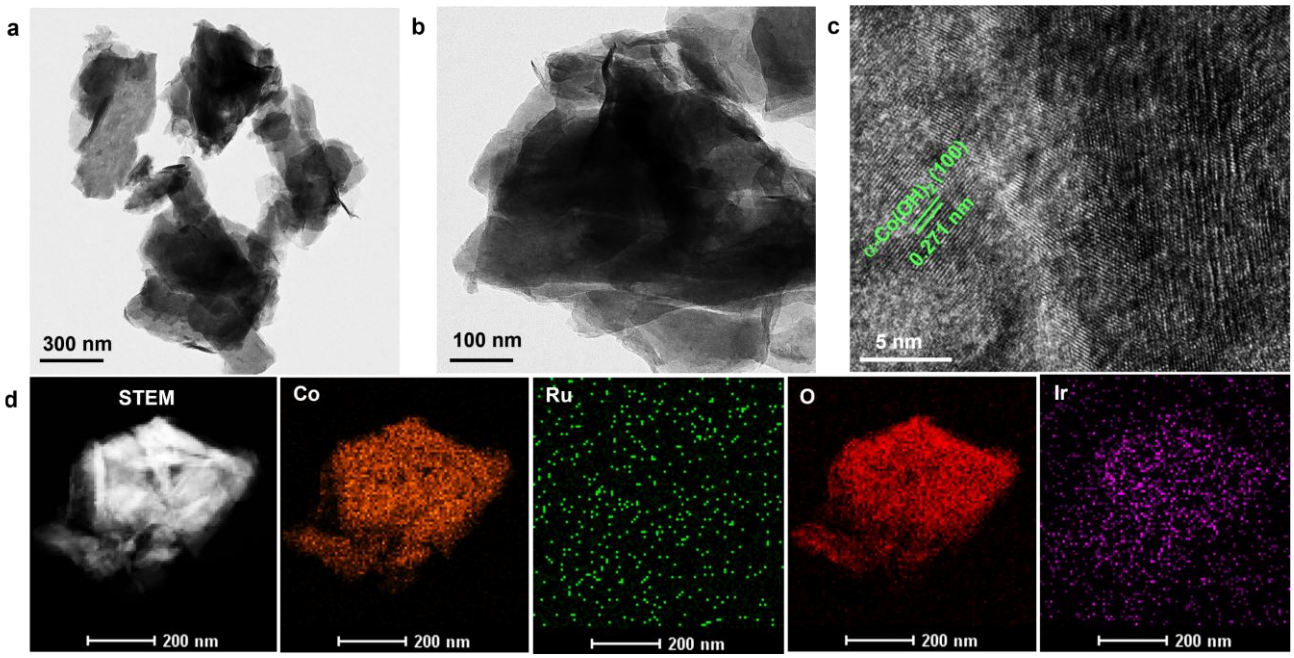

Figure S18. Structural characterization of Ru-IrO_x/α-$Co(OH)_2$catalyst after alkaline seawater oxidation stability evaluation. (a, b) TEM images, (c) HRTEM image, (d) STEM image of Ru-IrO_x/α-$Co(OH)_2$ catalyst after stability catalysis evaluation and corresponding EDS mappings of Co, Ir, Ru and O elements.

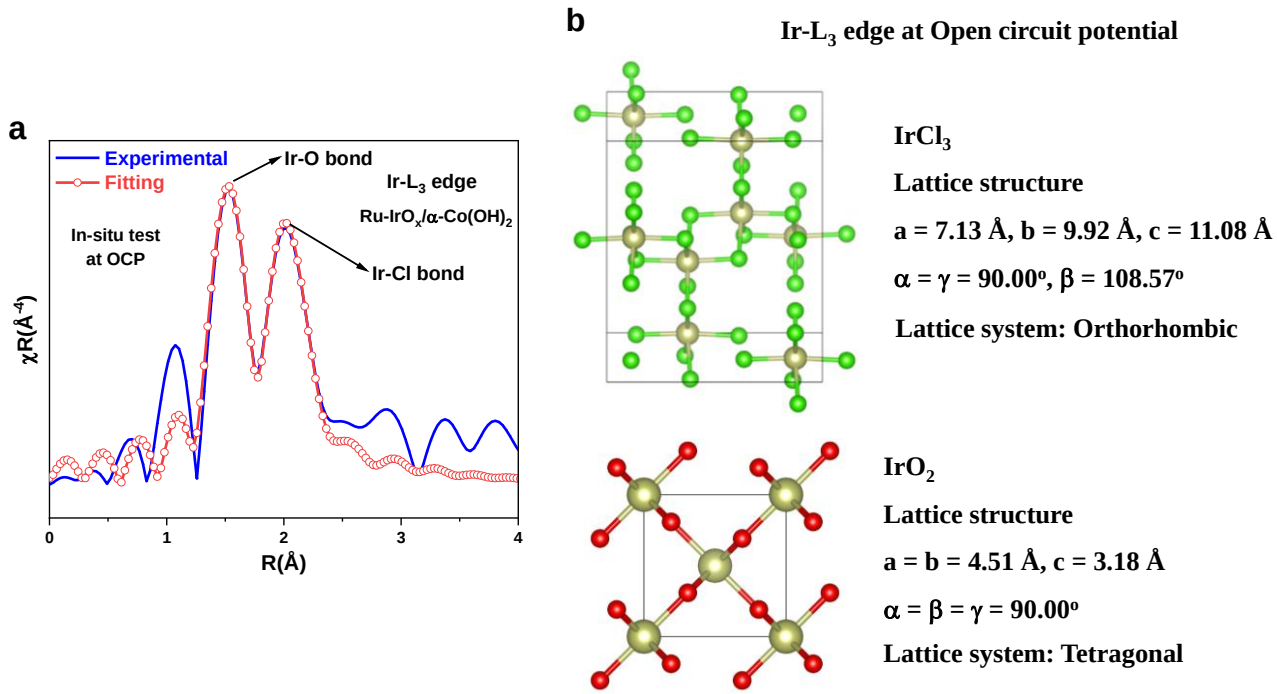

Figure S19. (a) Fitting curve for in-situ Ir-L_3 edge EXAFS spectra of Ru-IrO_x/α-$Co(OH)_2$ under open circuit potential. (b) The reference model orthorhombic $IrCl_3$ and tetragonal IrO_2 used for Ir-L_3 edge fitting at open circuit potential.

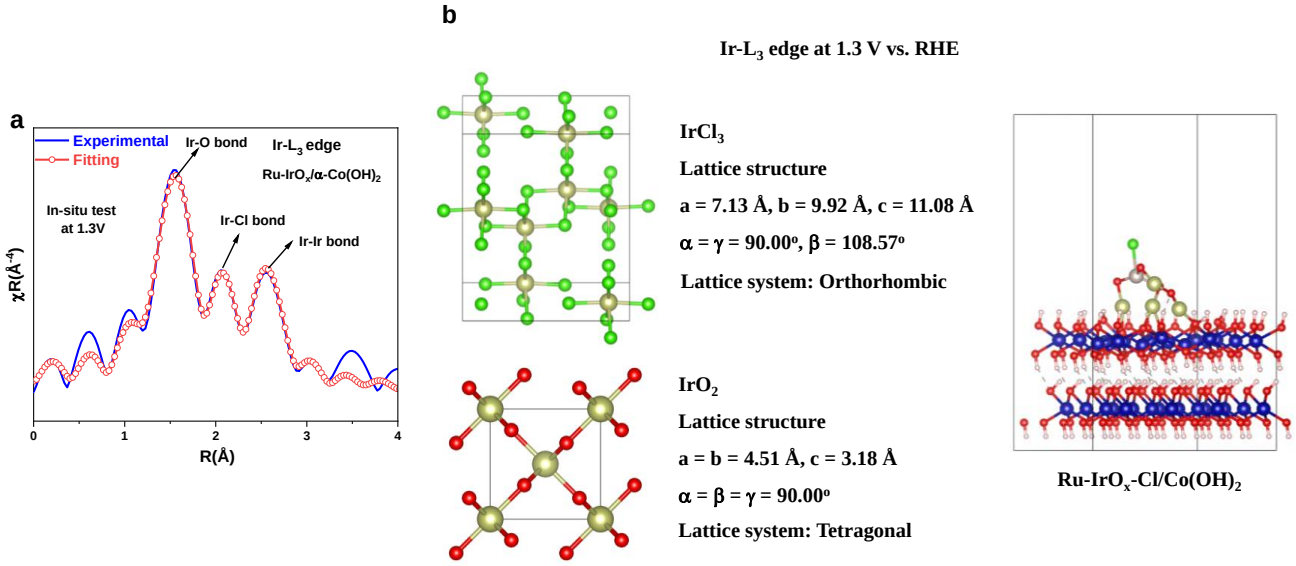

Figure S20. (a) Fitting curve for in-situ Ir-L_3 edge EXAFS spectra of Ru-IrO_x/α-$Co(OH)_2$ under 1.3 V vs. RHE. (b) The reference model orthorhombic $IrCl_3$, tetragonal IrO_2 and Ru-IrO_x-Cl/$Co(OH)_2$ used for Ir-L_3 edge fitting at 1.3 V vs. RHE.

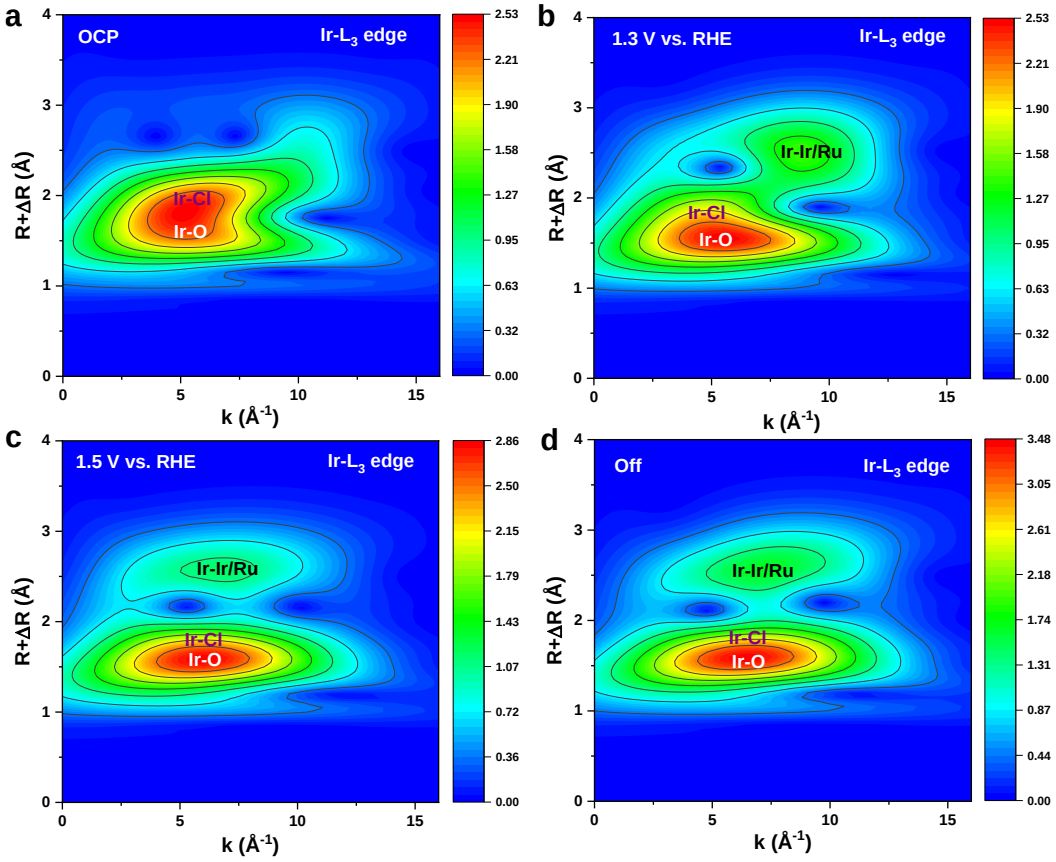

Figure S21. The wavelet transform of Ir-L_3 edge for Ru-IrO_x/α-$Co(OH)_2$ heterostructure under (a) OCP, (b) 1.30 V vs. RHE, (c) 1.50 V vs. RHE and (d) off voltage.

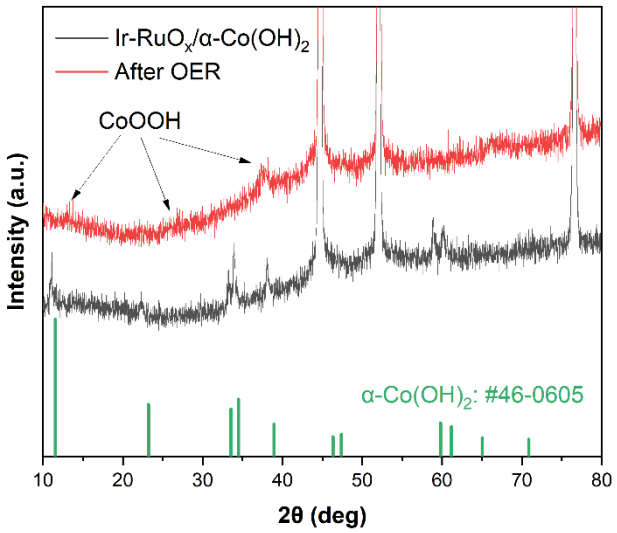

Figure S22. XRD patterns of Ru-IrO$_x$/α-Co(OH)$_2$ before and after OER.

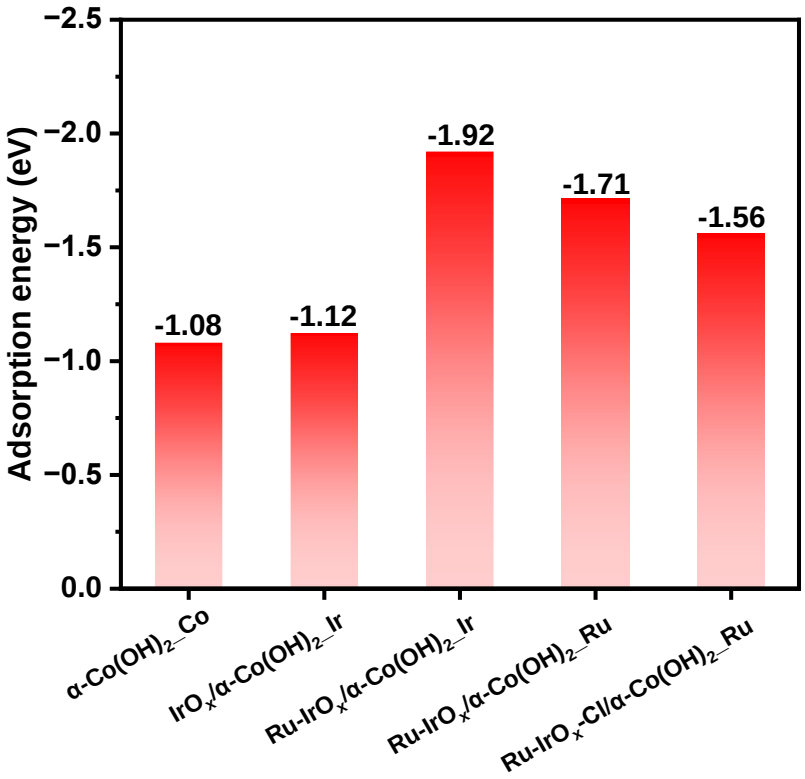

Figure S23. The adsorption energies of Cl^- ions on α-Co(OH)$_2$_Co, IrO$_x$/α-Co(OH)$_2$_Ir, Ru-IrO$_x$/α-Co(OH)$_2$_Ru, Ru-IrO$_x$/α-Co(OH)$_2$_Ir and Ru-IrO$_x$-Cl/α-Co(OH)$_2$_Ru.

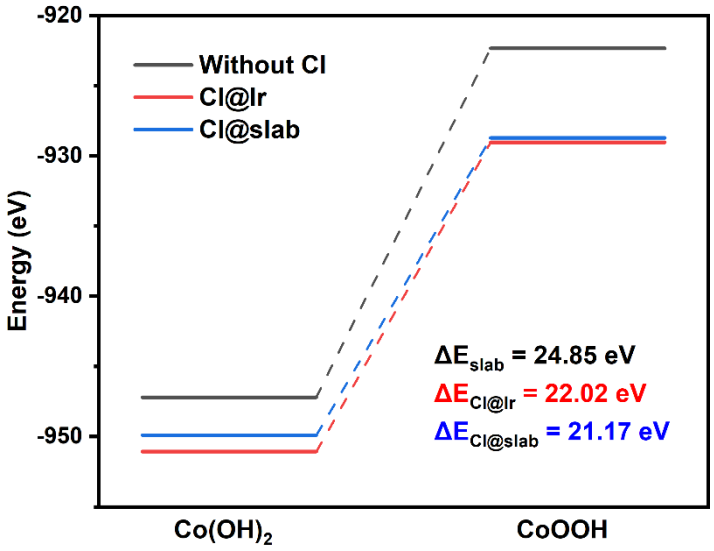

Figure S24. The energy barrier between Ru-IrO_x/α-$Co(OH)_2$ and Ru-IrO_x/CoOOH for three states: without Cl, Cl adsorbed on Ir and Cl adsorbed on substrate.

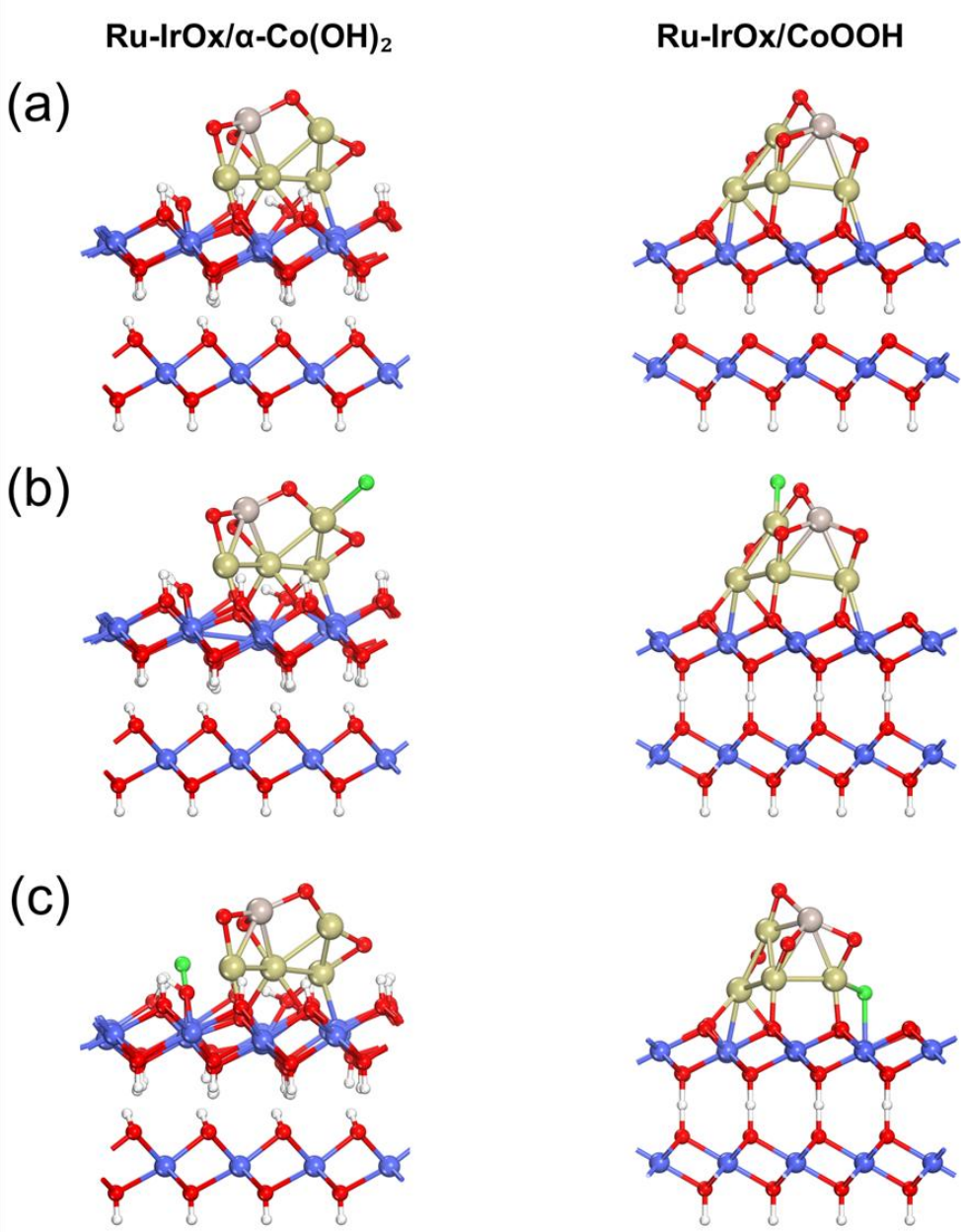

Figure S25. The structure of Ru-IrOx/α-$Co(OH)_2$ and Ru-IrOx/CoOOH for (a) unabsorbed Cl, (b) Cl adsorbed on Ir and (c) Cl adsorbed on substrate.

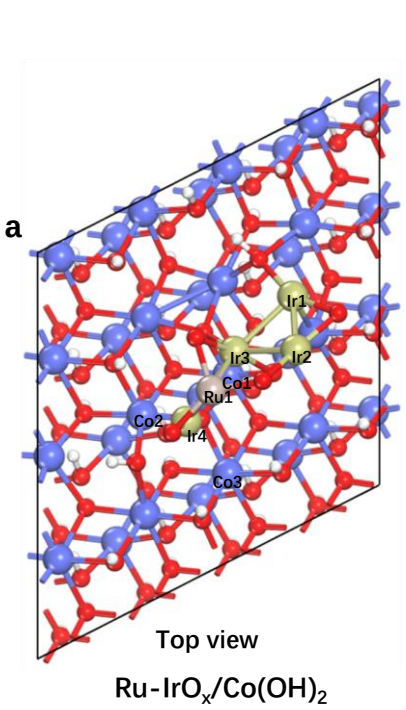

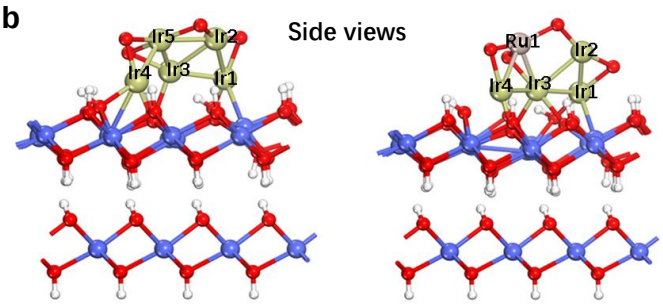

c

Atoms	$IrO_x/Co(OH)_2$	$Ru\text{-}IrO_x/Co(OH)_2$
Co1	1.274797	1.287213
Co2	1.22923	1.241133
Co3	1.264282	1.27394
Ir1	0.80478	0.466679
Ir2	0.77311	0.545305
Ir3	0.682126	0.851981
Ir4	0.436136	0.580789
	0.571144(Ir5)	1.159312(Ru)

Figure S26. (a) Top view of the visual image of constructed model Ru-IrO$_x$/Co(OH)$_2$. (b) Side view of the visual images of constructed models IrO$_x$/Co(OH)$_2$, Ru-IrO$_x$/Co(OH)$_2$. (c) The DFT calculated Balder charges of corresponding marked atoms adjacent to Ru, the Balder charge values in the listed table represent positive charges.

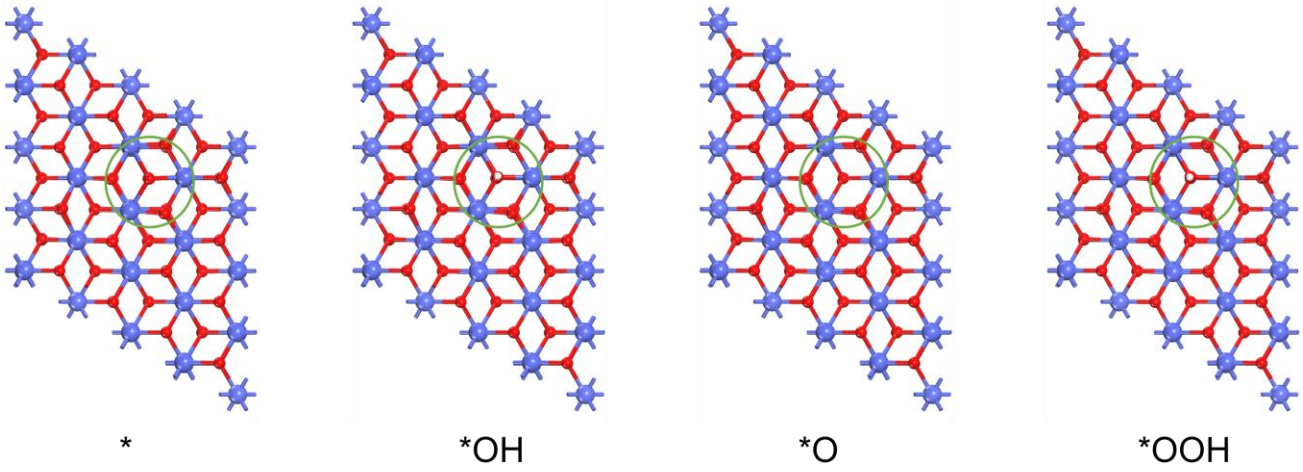

Figure S27. The side views of *, *OH, *O and *OOH on CoOOH.

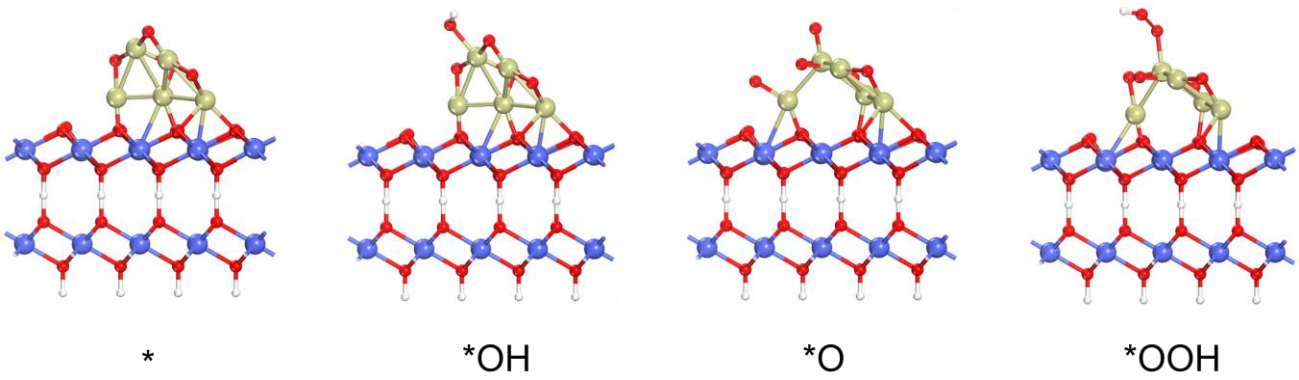

Figure S28. The side views of *, *OH, *O and *OOH on IrO_x/CoOOH.

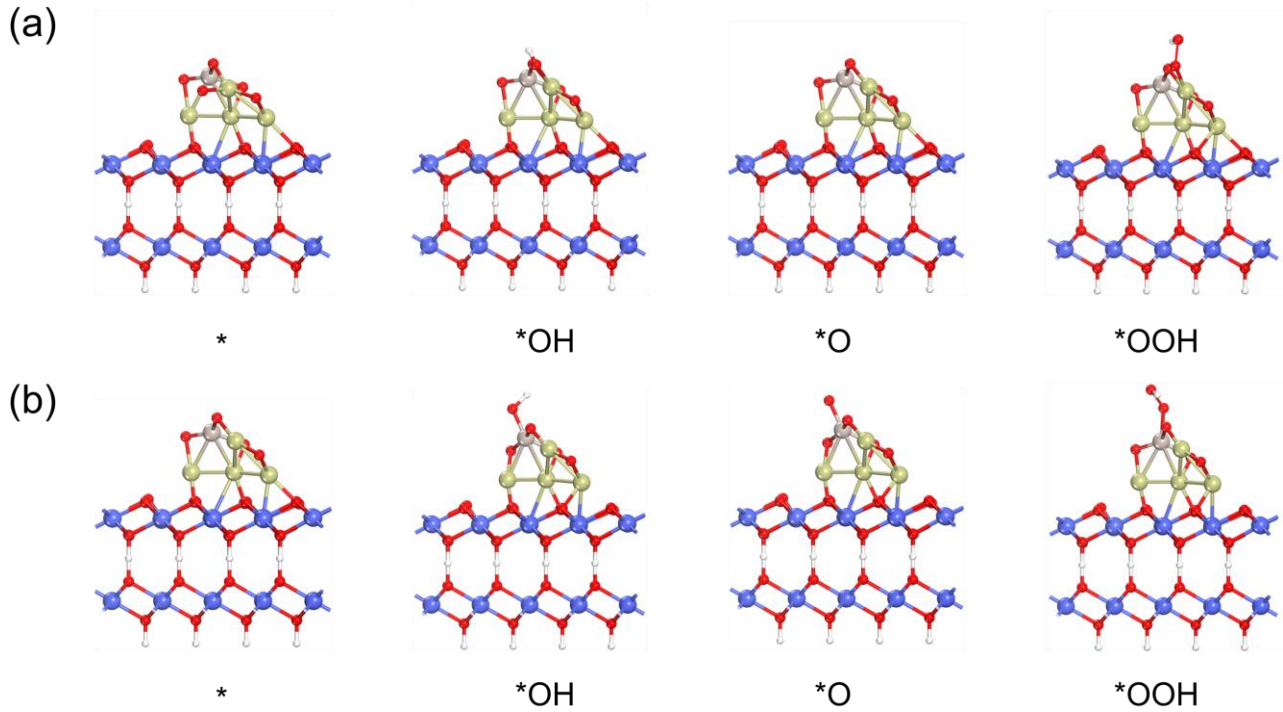

Figure S29. The side views of *, *OH, *O and *OOH on Ru-IrO_x/CoOOH. OER is performed on Ir (a) and Ru (b), respectively.

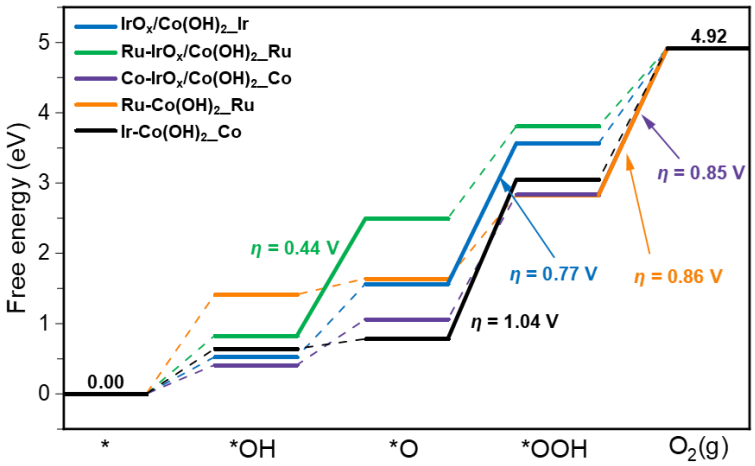

Figure S30. Gibbs free energy calculations for $IrO_x/Co(OH)_2$_Ir, Ru-$IrO_x/Co(OH)_2$_Ru, Co-$IrO_x/Co(OH)_2$_Co, Ru-$Co(OH)_2$_Ru and Ir-$Co(OH)_2$_Ir.

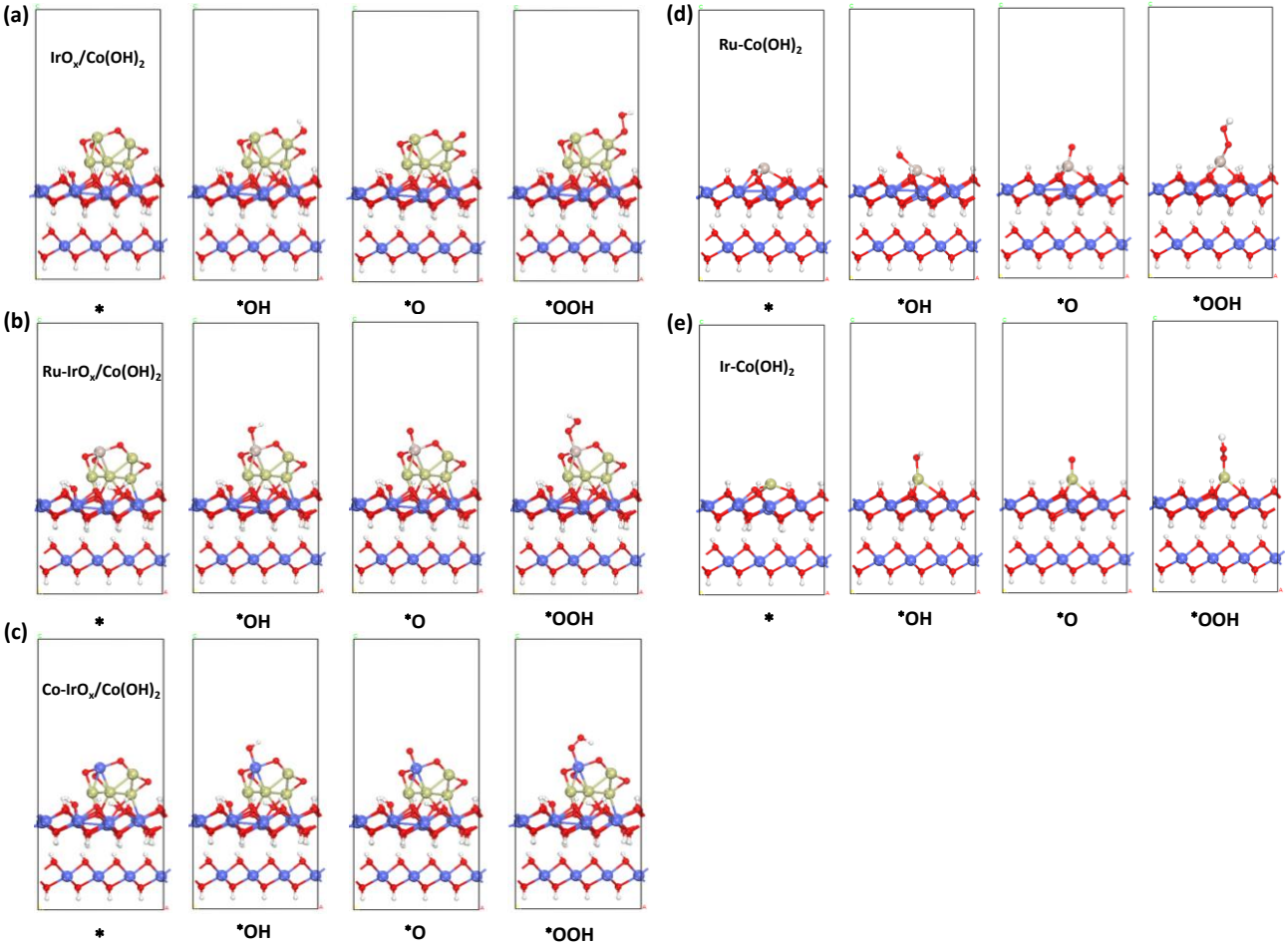

Figure S31. The model diagrams corresponding to the Gibbs free energy profiles in Figure S30. The sites where the calculations were performed for (a) $IrO_x/Co(OH)_2$, (b) Ru-$IrO_x/Co(OH)_2$, (c) Co-$IrO_x/Co(OH)_2$, (d) Ru-$Co(OH)_2$ and (e) Ir-$Co(OH)_2$ are Ir, Ru, Co, Ru and Ir, respectively.

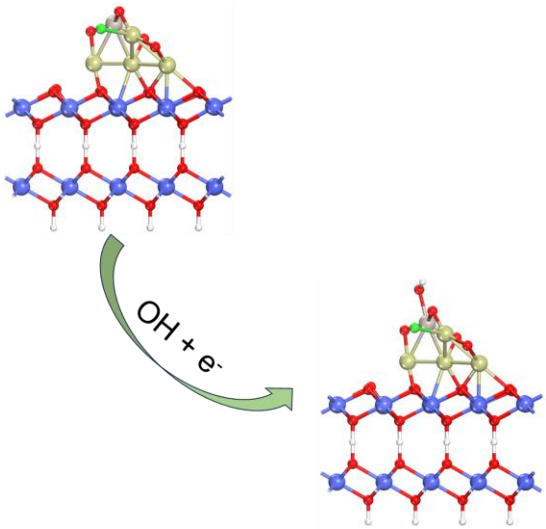

Figure S32. Optimized structure of *OH adsorption on Ru-IrO_x-Cl/CoOOH_Ru.

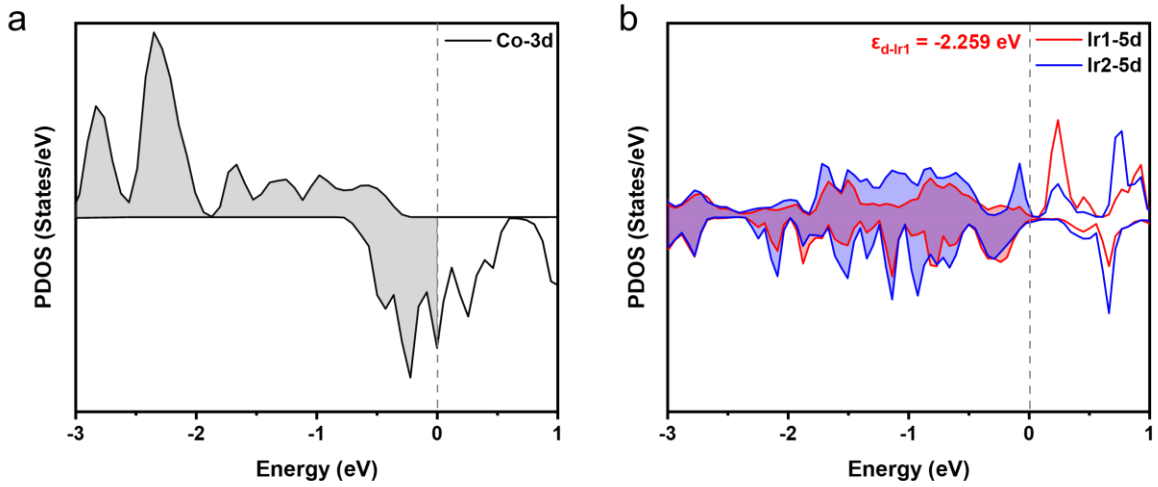

Figure S33. The PDOS of (a) CoOOH and (b) IrO_x/CoOOH.

Table S1. The detailed XPS fitting parameters of investigated catalysts.

Catalyst	Co 2p	Peak position (eV)	FWHM (eV)	Peak area	Peak area ratios	Constraints
Ru-IrO_x/α-$Co(OH)_2$	Co^{3+} $2p_{3/2}$	780.9	2.92	17982.4	32.6%	Double peak interval values set between 14.99 + 0.8 eV and 14.99 – 0.3 eV; FWHM values set between 0.50 eV and 3.50 eV; Lorentzian/Gaussian ratio value set as 30%
	Co^{2+} $2p_{3/2}$	782.4	3.50	11798.4	21.4%	
	Sat. ($2p_{3/2}$)	786.9	3.92	6771.2	12.3%	
	Co^{3+} $2p_{1/2}$	796.5	2.90	9148.9	16.6%	
	Co^{2+} $2p_{1/2}$	798.3	3.50	6064.1	10.9%	
	Sat. ($2p_{1/2}$)	802.8	3.92	3477.8	6.2%	
IrO_x/α-$Co(OH)_2$	Co^{3+} $2p_{3/2}$	781.3	2.47	17481.2	34.8%	
	Co^{2+} $2p_{3/2}$	783.2	3.51	8222.2	16.4%	
	Sat. ($2p_{3/2}$)	787.5	3.40	7478.7	14.8%	
	Co^{3+} $2p_{1/2}$	797.1	2.48	9099.1	18.1%	
	Co^{2+} $2p_{1/2}$	798.9	3.51	4147.7	8.2%	
	Sat. ($2p_{1/2}$)	803.2	3.40	3843.2	7.7%	
α-$Co(OH)_2$	Co^{3+} $2p_{3/2}$	780.9	2.08	43864.7	24.5%	
	Co^{2+} $2p_{3/2}$	782.7	3.23	46094.6	25.8%	
	Sat. ($2p_{3/2}$)	787.0	3.43	28763.8	16.1%	
	Co^{3+} $2p_{1/2}$	796.7	2.08	21632.2	12.1%	
	Co^{2+} $2p_{1/2}$	798.4	3.23	23704.2	13.2%	
	Sat. ($2p_{1/2}$)	802.7	3.43	14764.7	8.3%	

Catalyst	Ir 4f	Peak position (eV)	FWHM (eV)	Peak area	Peak area ratios	Constraints
IrO_x/α-$Co(OH)_2$	Ir^{4+} $4f_{7/2}$	62.6	1.63	5536.3	48.2%	Double peak interval values set between 3.20 + 0.2 eV and 3.20 – 0.1 eV; FWHM values set between 0.50 eV and 3.50 eV; Lorentzian/Gaussian ratio value set as 30%
	Ir^{4+} $4f_{5/2}$	65.7	1.63	4362.3	37.9%	
	Co 3p	60.5	1.79	1598.1	13.9%	
Ru-IrO_x/α-$Co(OH)_2$	Ir^{4+} $4f_{7/2}$	62.4	2.21	8867.5	50.1%	
	Ir^{4+} $4f_{5/2}$	65.6	2.21	6961.3	39.3%	
	Co 3p	60.6	2.78	1881.9	10.6%	
Catalyst	Ru 3d	Peak position (eV)	FWHM (eV)	Peak area	Peak area ratios	Constraints
Ru-IrO_x/α-$Co(OH)_2$	Ru^{4+} $3d_{5/2}$	284.0	1.25	1202.5	7.1%	Double peak interval values set between 4.10 + 0.3 eV and 4.10 – 0.1 eV; FWHM values set between 0.50 eV and 2.50 eV;
	C-C	284.8	1.23	6697.4	39.3%	

	Ru^{4+} $3d_{3/2}$	288.0	1.25	828.3	4.9%	Lorentzian/Gaussian ratio value set as 30%
	C-O	285.9	2.05	6297.7	37.0%	
	C=O	288.9	1.28	1991.1	11.7%	
Catalyst	O 1s	Peak position (eV)	FWHM (eV)	Peak area	Peak area ratios	Constraints
Ru-IrO_x/α-$Co(OH)_2$	M-OH	531.2	1.66	30608.5	63.9%	FWHM values set between 0.50 eV and 2.50 eV; Lorentzian/Gaussian ratio value set as 30%
	M-O	529.3	1.30	2327.8	4.9%	
	Oxygen vacancy	532.5	1.53	9719.3	20.3%	
	H-O-H	533.4	1.54	5246.3	10.9%	
IrO_x/α-$Co(OH)_2$	M-OH	531.5	1.60	14589.9	71.3%	
	M-O	529.6	2.41	978.6	4.8%	
	Oxygen vacancy	533.0	1.71	4143.1	20.2%	
	H-O-H	534.2	0.92	964.0	3.7%	
α-$Co(OH)_2$	M-OH	531.1	1.49	61272.3	74.0%	
	Oxygen vacancy	531.7	1.67	16414.4	19.8%	
	H-O-H	533.1	1.57	5070.2	6.2%	

Table S2. Curvefit parameters for Co-K edge EXAFS of Ru-IrO_x/α-$Co(OH)_2$ catalyst.

Path	d^b/Å	N	R/Å	ΔE_0/eV	σ^2/Å^2	R factor
Co-O1	2.043	0.3(1)	1.968	3.671	0.007(9)	0.0096
Co-O2	2.084	1.8(5)	2.172		0.007(9)	
Co-O3	2.151	2.7(8)	2.037		0.007(9)	
Co-Co1	3.115	1.7(9)	3.117		0.007(9)	
Co-Co2	3.254	0.9(3)	3.701		0.002(5)	
Co-Co3	3.320	2.7(8)	3.113		0.007(9)	

Table S3. Curvefit parameters for Ir-L_3 edge EXAFS of Ru-IrO_x/α-$Co(OH)_2$ catalyst.

Path	d^b/Å	N	R/Å	ΔE_0/eV	σ^2/Å^2	R factor
Ir-O1	1.969	2.0(7)	2.058	11.257	0.006(5)	0.0198
Ir-O2	2.041	4.1(4)	2.046		0.006(5)	
Ir-Ru	2.548	1.6(6)	2.406		0.006(1)	
Ir-Ir	2.574	5.3(8)	2.862		0.009(7)	

Table S4. Curvefit parameters for Ru-K edge EXAFS of Ru-IrO_x/α-$Co(OH)_2$ catalyst.

Path	d^b/Å	N	R/Å	ΔE_0/eV	σ^2/Å^2	R factor
Ru-O	2.103	4.8(7)	2.016	8.991	0.007(7)	0.0196

Table S5. Comparison for the catalytic performance of alkaline seawater oxidation with recently reported representative electrocatalysts.

Catalysts	Electrolyte	Overpotential	Durability	Reference
Ru-IrO_x/α-$Co(OH)_2$	1.0 M KOH + seawater	206 mV at 100 mA cm^{-2}	310 h at 500 mA cm^{-2}	*This work*
Ru-Ni_2P/Fe_2P	1.0 M KOH + Seawater	331 mV at 1000 mA cm^{-2}	100 h at 500 mA cm^{-2}	*Adv. Funct. Mater*. **2024**, *34*, 2400734.
Ru Sas-MoO_{3-x}/NF	1.0 M KOH + seawater	529 mV at 100 mA cm^{-2}	60 h at 50 mA cm^{-2}	*Adv. Sci.* **2023**, *10*, 2300342.
Ru_2Co_1BO-350	1.0 M KOH + seawater	219 mV at 10 mA cm^{-2}	20 h at 10 mA cm^{-2}	*Nano Lett.* **2023**, *23*, 1052-1060.
NiIr-LDH	1.0 M KOH + seawater	361 mV at 500 mA cm^{-2}	650 h at 500 mA cm^{-2}	*J. Am. Chem. Soc.* **2022**, *144*, 9254-9263.
Ru-CoO_x/NF	1.0 M KOH + seawater	630 mV at 100 mA cm^{-2}	10000 CV cycles to 1000 mA cm^{-2}	*Small* **2021**, *17*, 2102777.
Ni/$Co(OH)_2$-Ru@NF	1.0 M KOH + seawater	180 mV at 10 mA cm^{-2}	—	*Small* **2025**, *21*, 2410086.
$Ru_{22}NiMoP_2$/NF	1.0 M KOH + seawater	240 mV at 10 mA cm^{-2}	10 h at 10 mA cm^{-2}	*Sustainable Energy Fuels*, **2023**,*7*, 4677-4686.
Ru-BO_x-OH-300	1.0 M KOH + 3.5 wt.% NaCl	235 mV at 10 mA cm^{-2}	20 h at 10 mA cm^{-2}	*Energy Environ Sci.* **2024**, *17*, 3888-3897.
Ru-CoP_2	1.0 M KOH+ seawater	350 mV at 100 mA cm^{-2}	180 h at 500 mA cm^{-2}	*J. Energy Chem.* **2025**, *100*, 317-

				326.
Ru/NiFeOOH/NFF	1.0 M KOH + seawater	270 mV at 100 mA cm^{-2}	100 h at 100 mA cm^{-2}	*Chem. Eng. J.* **2023**, *458*, 141457.
RuO_2–Ti_3C_2/NF	1.0 M KOH + seawater	378 mV at 100 mA cm^{-2}	40 h at 20 mA cm^{-2}	*ACS Appl. Mater. Interfaces.* **2023**, *15*, 58345-58355.
cRu-Ni_3N	1.0 M KOH + seawater	390 mV at 50 mA cm^{-2}	10 h at 10 mA cm^{-2}	*Energy Environ. Mater.* **2023**, *6*, e12318.
Ru SAs-MoO_{3-x}/NF	1.0 M KOH + seawater	529 mV at 100 mA cm^{-2}	60 h at 40 mA cm^{-2}	*Adv. Sci.* **2023**, *10*, 2300342.
Ir/CoFe-LDH	6.0 M NaOH + 2.8 M NaCl	202 mV at 10 mA cm^{-2}	1000 h at 800 mA cm^{-2}	*Nat. Commun.* **2024**, *15*, 1973.
CAPist-S1	1 M KOH + seawater	220 mV at 1.0 A cm^{-2}	Over 9000 h at 1 A cm^{-2}	*Adv. Sci.* **2025**, *12*, 2416661.
$B_4O_5(OH)_4^{2-}$–CoFe-LDH/SO_4^{2-}–$CoMoO_4$ nanohybrid	1.0 M KOH + seawater	370 mV at 1.0 A cm^{-2}	120 h at 40 mA cm^{-2}	*Chem. Sci.* **2025**, *16*, 15684.
VO_4^{3-}-NiFe LDH/VO_x/NF	1.0 M KOH + 0.6 M NaCl	220 mV at 100 mA cm^{-2}	2500 h at 1000 mA cm^{-2} in 1.0 M KOH + seawater	*Chem. Sci.,* **2026**,*17,* 214-224.

Table S6. Curvefit parameters for Ir-L_3 edge EXAFS of in-situ tested Ru-IrO_x/α-$Co(OH)_2$ catalyst at open circuit potential.

Path	d^b/Å	N	R/Å	ΔE_0/eV	σ^2/Å^2	R factor
Ir-O	2.002	2.9(2)	1.982	6.489	0.002(0)	0.0200
Ir-Cl	2.362	2.0(5)	2.354	9.522	0.002(4)	

Table S7. Curvefit parameters for Ir-L_3 edge EXAFS of in-situ tested Ru-IrO_x/α-$Co(OH)_2$ catalyst at 1.3V vs. RHE.

Path	d^b/Å	N	R/Å	ΔE_0/eV	σ^2/Å^2	R factor
Ir-O	2.002	5.3(2)	1.983	8.224	0.010(2)	0.0029
Ir-Cl	2.361	1.9(9)	2.464	10.532	0.008(2)	
Ir-Ir	2.544	6.6(5)	2.556	-4.530	0.008(1)	

References

[1] Y. Xue, B. Huang, Y. Yi, Y. Guo, Z. Zuo, Y. Li, Z. Jia, H. Liu, Y. Li, *Nat. Commun*. 2018, **9**, 1460.

[2] H. Su, W. Zhou, W. Zhou, Y. Li, L. Zheng, H. Zhang, M. Liu, X. Zhang, X. Sun, Y. Xu, F. Hu, J. Zhang, T. Hu, Q. Liu, S. Wei, *Nat. Commun.* 2021, **12**, 6118.